Lab on a Chip

PAPER

View Article Online
View Journal | View Issue

Cite this: *Lab Chip*, 2014, **14**, 2824

Investigation of acoustic streaming patterns around oscillating sharp edges†

Nitesh Nama,[a] Po-Hsun Huang,[a] Tony Jun Huang*[ab] and Francesco Costanzo*[ac]

Received 12th February 2014,
Accepted 17th April 2014

DOI: 10.1039/c4lc00191e

www.rsc.org/loc

Oscillating sharp edges have been employed to achieve rapid and homogeneous mixing in microchannels using acoustic streaming. Here, we used a perturbation approach to study the flow around oscillating sharp edges in a microchannel. This work extends prior experimental studies to numerically characterize the effect of various parameters on the acoustically induced flow. Our numerical results match well with the experimental results. We investigated multiple device parameters such as the tip angle, oscillation amplitude, and channel dimensions. Our results indicate that, due to the inherent nonlinearity of acoustic streaming, the channel dimensions could significantly impact the flow patterns and device performance.

1 Introduction

Microfluidic devices can be effective in many applications including biomedical diagnostics, drug delivery, chemical synthesis, and enzyme reactions.[1] An important requirement for these systems is the ability to rapidly and efficiently mix small amounts of samples on a microscale.[2,3] Various techniques have been utilized to enable rapid mixing in microfluidic devices including chaotic advection,[4–9] hydrodynamic focusing,[10,11] electrokinetically driven mixing,[12–16] 3D combinatorial bubble-based mixing,[17,18] and thermally-[19,20] as well as optically-induced[21] mixing. Recently, acoustic-based mixers[22–26] have gained significant interest because of their non-invasive nature. These mixers utilize acoustic waves to perturb the laminar flow pattern in microchannels to achieve rapid and homogeneous mixing.[27–32] In particular, acoustically driven, oscillating bubbles have been used to achieve fast and homogeneous mixing by generating acoustically-induced microvortices.[33–35] Bubble-based acoustic mixers have been utilized for enzyme reaction characterization,[36] DNA hybridization enhancement,[37,38] chemical gradient generation,[39] and optofluidic modulators.[40,41] However, bubble-based acoustic mixers have also proven to be somewhat challenging due to bubble instability, heat generation, and hard-to-control bubble-trapping processes.[41,42] To overcome these difficulties, we recently reported a sharp-edge-based micro-mixer[41] where the flow field is perturbed using microvortices generated by an acoustically oscillating sharp edge. The performance of the sharp-edge based micro-mixer was found to be very close to that of the bubble-based micro-mixer with the added advantage of convenient and stable operation over bubble-based micro-mixers. However, to realize the full potential of these devices and explore further applications, a deeper understanding of the flow field around oscillating sharp edges is required.

Steady streaming around obstacles in an oscillating incompressible fluid has been studied extensively.[43–47] Due to the dissipative nature of the fluid, the response to time-harmonic forcing is generally not harmonic. The fluid's response to harmonic forcing can be viewed as a combination of a time harmonic response, generally referred to as acoustic response, and the remainder, referred to as acoustic streaming.[48] Time averaging of the Navier–Stokes equations yields a term analogous to Reynolds stress (normally observed in turbulent flows) which causes a "slow" steady streaming around obstructions in the flow field. This can also be interpreted by saying that the nonlinear hydrodynamic coupling results in a partial transmission of the acoustic wave energy to the fluid as steady momentum resulting in acoustic streaming.[49] Since the latter is a byproduct of the acoustic attenuation due to viscous dissipation, it provides a unique way to utilize the dominant viscous nature of microfluidic flows.[50] It is important to note that there are two main dissipation mechanisms:[43] (1) wave attenuation in the bulk fluid, and (2) dissipation in the boundary, in which the streaming in the boundary layer drives streaming in the bulk. Both mechanisms owe their origin to the action of Reynolds stress.[43,45] It is the acoustic energy flux dissipation that

[a] *Department of Engineering Science and Mechanics, The Pennsylvania State University, University Park, PA 16802, USA. E-mail: junhuang@psu.edu*
[b] *Department of Bioengineering, The Pennsylvania State University, University Park, PA 16802, USA*
[c] *Center for Neural Engineering, The Pennsylvania State University, University Park, PA 16802, USA. E-mail: costanzo@engr.psu.edu*

† Electronic supplementary information (ESI) available. See DOI: 10.1039/c4lc00191e

induces momentum flux gradients, and these, in turn, drive acoustic streaming. While, in the first case, dissipation occurs in the bulk fluid, in the second case, most of the dissipation occurs within the boundary layers at the solid surfaces.[51] The dominance of one mechanism over the other is dependent on the size of the device. For devices where the microchannel is very small compared to the wavelength and the attenuation length, like the one used in this article, the streaming will be boundary layer driven.

While bubble-based mixers have been extensively studied both analytically and numerically,[33,37,52,53] the knowledge of flow fields around oscillating sharp edges is limited. Lieu *et al.*[49] have studied the flow around obstacles in an oscillating incompressible flow field. However, Lieu *et al.*[49] do not discuss the possible singularities induced in the flow by the geometry of the obstacles. In addition, their analysis is not directly applicable to our system, which is characterized by acoustic wave propagation, with the latter requiring an explicit modeling of the fluid compressibility. Although steady streaming has been widely studied for cases where the fluid can be treated as infinite, little attention has been given to this phenomenon in confined flows.[49] The basic hydrodynamic traits of low Reynolds number flows in microfluidic channels are dictated by the motion of the walls. This, coupled with the inherent nonlinearity of the acoustic streaming phenomenon, implies that the geometrical dimensions of the microfluidic channel and the boundary conditions significantly impact the flow field around the oscillating sharp edge inside a microchannel. These considerations justify a numerical approach to study the flows in question in which the geometry of the walls can be accurately represented.

In this work, we numerically investigate the acoustic streaming generated in a fluid by oscillating sharp edges inside a microchannel. We build on our previous experimental studies and aim at characterizing the effect of various parameters on the micro-eddies around the sharp edges. We model the fluid as compressible and linear viscous so that the fluid's equations of motion are the compressible Navier–Stokes equations. These are intrinsically nonlinear and characterized by different behaviors over wide ranges of time and length scales. The flow on the large length- and time-scales arises from the acoustic excitation on much smaller time and length scales.[28] Consequently, a direct solution of the compressible Navier–Stokes equation remains computationally challenging even with modern computational tools. To overcome this difficulty, we employ Nyborg's perturbation approach[51] complemented by periodic boundary conditions. To capture the singularity in the flow field, we refine the mesh near the tip of the sharp edge using an adaptive mesh refinement strategy. Our approach is general in the sense that we do not make *a priori* assumptions about specific flow regimes in selected regions of the computational domain. After identifying boundary conditions that lead to predictions matching the experimental observations, we numerically investigate the effects of various parameters like tip angle, displacement amplitude, and channel dimensions on the streaming velocity and particle mean trajectories. The numerical methods and results presented in this article will be useful in optimizing the performance of acoustofluidic devices and providing design guidelines.

2 Micro-acousto-fluidic channel with sharp edges

Fig. 1(a) provides a schematic of the oscillating sharp-edge-based acoustofluidic micromixer. A single-layer polydimethylsiloxane (PDMS) channel with eight sharp-edges on its sidewall (four on each side) was fabricated using standard soft lithography and bonded onto a glass slide. A piezoelectric transducer (model no. 273-073, RadioShack®) was then attached adjacent to the PDMS channel. Upon the actuation of the piezoelectric transducer, the sharp-edges were acoustically oscillated with a frequency of 4.75 kHz. These oscillations generate a pair of counter-rotating vortices (double-ring recirculating flows) in the fluid around the tip of each sharp-edge, as shown in Fig. 1(b). Typical channel dimensions are indicated in Fig. 1(c). To visualize and characterize the streaming flow inside the channel, a solution containing 1.9 μm diameter dragon green fluorescent beads (Bangs Laboratories, Inc.™) was introduced into the channel. The typical bead trajectories observed in experiments are shown in Fig. 2.

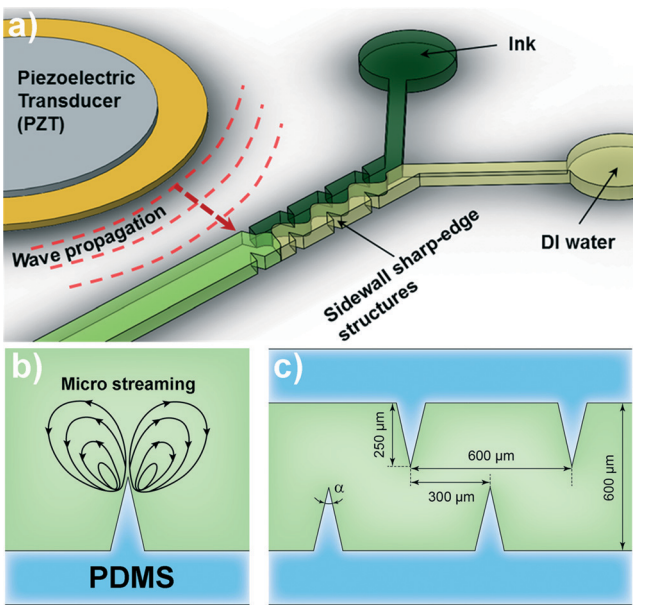

Fig. 1 (a) Schematic of the device showing a microfluidic channel with sharp-edge structures on its side walls. The channel walls are subjected to a time-harmonic excitation produced by a piezoelectric transducer placed on one side of the channel. (b) Typical micro streaming patterns produced in the fluid occupying the channel as a response to piezoelectric excitation. (c) Typical geometric dimensions of the corrugated channel.

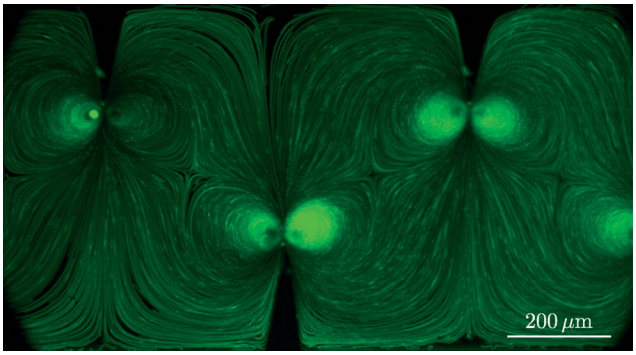

Fig. 2 Experimentally observed trajectories of 1.9 μm diameter fluorescent polystyrene beads in our acoustically oscillated micromixer with sharp edges. The geometry of the microchannel is described in Fig. 1(c) except for the fact that here, the tips of the sharp edges are 200 μm from the wall instead of 250 μm. The driven oscillation is harmonic with a frequency equal to 4.75 kHz.

3 Modeling

We denote vector quantities by boldface type and scalars by a normal-weight font.

The mass and momentum balance laws governing the motion of a linear viscous compressible fluid are[48,54,55]

$$\frac{\partial \rho}{\partial t} + \nabla\cdot(\rho \mathbf{v}) = 0 \tag{1}$$

and

$$\rho\frac{\partial \mathbf{v}}{\partial t} + \rho(\mathbf{v}\cdot\nabla)\mathbf{v} = -\nabla p + \mu\nabla^2\mathbf{v} + \left(\mu_b + \frac{1}{3}\mu\right)\nabla(\nabla\cdot\mathbf{v}), \tag{2}$$

where ρ is the mass density, $\mathbf{v}$ is the fluid velocity, p is the fluid pressure, and μ and μ_b are the shear and bulk dynamic viscosities, respectively. The fields ρ, p, and $\mathbf{v}$ are understood to be in Eulerian form,[54] *i.e.*, functions of time t and of the spatial position $\mathbf{x}$ within a chosen control volume. Eqn (1) and (2), with appropriate boundary conditions and a constitutive relation linking the pressure to the fluid density, allow one to predict the motion of the fluid. We assume the relation between p and ρ to be linear:

$$p = {c_0}^2\rho, \tag{3}$$

where c_0 is the speed of sound in the fluid at rest. Direct simulation of this non-linear system of equations poses significant numerical challenges owing to the widely separated length (characteristic wave lengths *vs.* the characteristic geometrical dimensions of the microfluidic channels) and time scales (characteristic oscillation periods *vs.* characteristic times dictated by the streaming speed).[56] Because of viscous dissipation, the response of the fluid to harmonic forcing is, in general, not harmonic. The fluid response is generally thought to be composed of two components: (i) a periodic component with a period equal to the forcing period, and (ii) a remainder that can be viewed as being steady. It is this second component which is generally referred to as the streaming motion.[48] We employ the Nyborg's perturbation technique[51] in which the fluid velocity, density, and pressure are assumed to have the following form:

$$\mathbf{v} = \mathbf{v}_0 + \varepsilon\tilde{\mathbf{v}}_1 + \varepsilon^2\tilde{\mathbf{v}}_2 + O(\varepsilon^3)\cdots, \tag{4a}$$

$$p = p_0 + \varepsilon\tilde{p}_1 + \varepsilon^2\tilde{p}_2 + O(\varepsilon^3) + \cdots, \tag{4b}$$

$$\rho = \rho_0 + \varepsilon\tilde{\rho}_1 + \varepsilon^2\tilde{\rho}_2 + O(\varepsilon^3) + \cdots, \tag{4c}$$

where ε is a non-dimensional smallness parameter. Following Köster,[57] we define ε as the ratio between the amplitude of the displacement of the boundary in contact with the piezoelectrically driven substrate (*i.e.*, the amplitude of the boundary excitation) and the characteristic length. We take the 0-th order velocity field $\mathbf{v}_0$ to be equal to zero thus assuming the absence of an underlying net flow along the micro-channel.

$$\begin{aligned} \mathbf{v}_1 &= \varepsilon\tilde{\mathbf{v}}_1, \quad p_1 = \varepsilon\tilde{p}_1, \quad \rho_1 = \varepsilon\tilde{\rho}_1, \\ \mathbf{v}_2 &= \varepsilon^2\tilde{\mathbf{v}}_2, \quad p_2 = \varepsilon^2\tilde{p}_2, \quad \rho_2 = \varepsilon^2\tilde{\rho}_2, \end{aligned} \tag{5}$$

Substituting eqn (4) into eqn (1) and (2) and setting the sum of all the terms of order one in ε to zero, the following problem, referred to as the first-order problem, is obtained:

$$\frac{\partial \rho_1}{\partial t} + \rho_0(\nabla\cdot\mathbf{v}_1) = 0, \tag{6}$$

$$\rho_0\frac{\partial \mathbf{v}_1}{\partial t} = -\nabla p_1 + \mu\nabla^2\mathbf{v}_1 + \left(\mu_b + \frac{1}{3}\mu\right)\nabla(\nabla\cdot\mathbf{v}_1). \tag{7}$$

Repeating the above procedure for the terms of order two in ε, and averaging the resulting equations over a period of oscillation, the following set of equations, referred to as the second-order problem, is obtained:

$$\left\langle\frac{\partial \rho_2}{\partial t}\right\rangle + \rho_0\nabla\cdot\langle\mathbf{v}_2\rangle = -\nabla\cdot\langle\rho_1\mathbf{v}_1\rangle, \tag{8}$$

$$\begin{aligned} &\rho_0\left\langle\frac{\partial \mathbf{v}_2}{\partial t}\right\rangle + \left\langle\rho_1\frac{\partial \mathbf{v}_1}{\partial t}\right\rangle + \rho_0\langle\mathbf{v}_1\cdot\nabla\mathbf{v}_1\rangle \\ &\quad = -\nabla\langle p_2\rangle + \mu\nabla^2\langle\mathbf{v}_2\rangle + \left(\mu_b + \frac{1}{3}\mu\right)\nabla\nabla\cdot\langle\mathbf{v}_2\rangle, \end{aligned} \tag{9}$$

where $\langle x\rangle$ denotes the time average of the quantity x over a full oscillation time period. As pointed out by Stuart,[45,58] inertia terms in eqn (9) can be significant and must be retained in the formulation. Also, to fully account for viscous attenuation of the acoustic wave, both within and without the boundary layer, the last term in eqn (9) associated with the bulk viscosity must also be retained. The above sets of equations need to be complemented by appropriate boundary conditions. In Fig. 1(a) and 3, we observe that the device

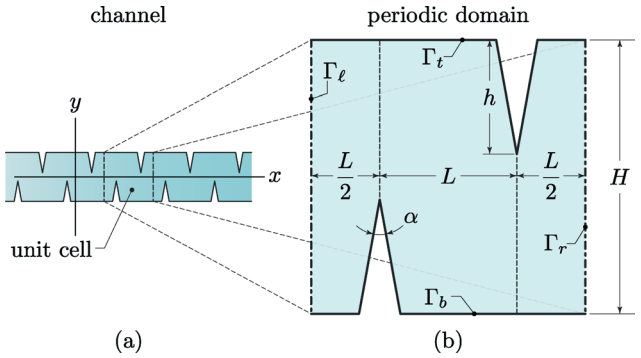

Fig. 3 (a) A portion of the microfluidic device. (b) Definition of a periodic cell forming the device.

consists of an assemblage of identical cells. While the number of cells in a device is finite, we assumed that the flow in each cell is identical to the flow in any other cell, and therefore we used the cell in Fig. 3(b) as our computational domain with the stipulation that computed flow must satisfy periodic boundary conditions. As will be discussed later, the solution of the streaming problem under periodic boundary conditions predicted flows that agreed well with those experimentally observed. The latter also have an anti-symmetric pattern internal to the selected unit cell corresponding to the region of width L in Fig. 3(b). In these figures, we have also indicated the relevant geometric descriptors that define our solution domain as well as the labels identifying specific regions of the boundary.

3.1 Boundary conditions

The action of the transducer is transferred onto the fluid in the microchannel by way of the device's substrate and the channel's PDMS walls. PDMS has an acoustic impedance similar to that of water. A precise modeling of the loading acting on the fluid would require the solution of a 3D piezo-electro-elastic problem. With this in mind, we note that the purpose of this work is to investigate how various features of sharp-edge micro-acousto-fluidic devices contribute to mixing. This objective can be achieved without detailed modeling of wave propagation through the substrate and its passage through the channel walls by subjecting the walls of the channel to appropriate boundary conditions. This would also allow us to solve a 2D instead of a 3D problem. While identifying an appropriate set of boundary conditions is generally difficult, the task is simplified by the availability of experimental results concerning typical flows observed in the devices. As mentioned earlier, our group has generated a significant amount of experimental results (Fig. 2) which were published by Huang *et al.*[41] Hence, in this work, we do not solve a coupled piezo-electro-elastic problem to relate the voltage control on the transducer to the corresponding loading conditions on the channel. Rather, we formulate simple boundary conditions based on observations from our prior experimental work.[41] In Fig. 1(a) and 3, we observe that the diameter of the transducer is much larger than the transverse width of the channel (≈600 μm) so the channel can be assumed to be subject to a plane wave parallel to the x direction and traveling in the y direction. It must be noted that this assumption cannot be used if the wavelength of the acoustic wave is comparable to the channel dimensions. In that case, one needs to consider the radial nature of the acoustic wave. In the device used in this article, the wavelength of the acoustic wave (≈30 cm) is much larger than the channel width (≈600 μm). Hence, we assume that the boundary portions Γ_t and Γ_b (the solid lines in Fig. 3(b), including the sharp edge structures) are subject to a displacement field $\mathbf{w}(\mathbf{x}, t)$ of the following form

$$\begin{aligned}\mathbf{w}(x_t,t) &= \mathbf{w}_c^t\cos(2\pi ft) + \mathbf{w}_s^t\sin(2\pi ft),\\ \mathbf{w}(x_b,t) &= \mathbf{w}_c^b\cos(2\pi ft) + \mathbf{w}_s^b\sin(2\pi ft),\end{aligned} \tag{10}$$

where $\mathbf{w}_c^t$, $\mathbf{w}_c^b$, $\mathbf{w}_s^t$, and $\mathbf{w}_s^s$ are vector-valued constants, and where f is the transducer oscillation frequency in hertz. Consistent with the asymptotic expansion in eqn (4), the boundary conditions on Γ_t and Γ_b for the first-order problem are[57,59] $\mathbf{v}_1(\mathbf{x}_{t,b}, t) = \partial\mathbf{w}(\mathbf{x}_{t,b}, t)/\partial t$, which gives

$$\mathbf{v}_1(\mathbf{x}_{t,b}, t) = -2\pi f[\mathbf{w}_c^{t,b}\sin(2\pi ft) - \mathbf{w}_s^{t,b}\cos(2\pi ft)], \tag{11}$$

where the subscripts and superscripts t and b stand for 'on Γ_t' and 'on Γ_b', respectively.

For the second-order problem, we have[57,59]

$$\mathbf{v}_2(\mathbf{x}_{t,b}, t) = -\langle(\mathbf{w}(\mathbf{x}_{t,b}, t)\cdot\nabla)\mathbf{v}_1(\mathbf{x}_{t,b}, t)\rangle. \tag{12}$$

As already mentioned, and as shown in Fig. 2 and 3, experimental results are characterized by distinctive symmetries. Hence, for both the first- and second-order problems, we enforce periodic boundary conditions along the x direction, that is, on Γ_ℓ and Γ_r. Specifically, for all pairs of homologous points $\mathbf{x}_\ell$ and $\mathbf{x}_r$ on Γ_ℓ and Γ_r, respectively, we demand that

$$\mathbf{v}_1(\mathbf{x}_\ell, t) = \mathbf{v}_1(\mathbf{x}_r, t) \text{ and } \mathbf{v}_2(\mathbf{x}_\ell, t) = \mathbf{v}_2(\mathbf{x}_r, t). \tag{13}$$

As far as the y direction is concerned, we observe that the wavelength of the forced oscillations in the substrate is much larger than the channel's width. Hence, we subject Γ_t and Γ_b to identical (uniform) boundary conditions as though the channel walls were rigidly and harmonically displaced in the vertical direction:

$$\mathbf{w}(\mathbf{x}_b, t) = \mathbf{w}(\mathbf{x}_t, t). \tag{14}$$

For comparison purposes, noticing that the experiments suggest the presence of an anti-symmetric pattern relative to the vertical mid-line of the solution domain, we have also considered the following boundary conditions:

$$\mathbf{w}(\mathbf{x}_b, t) = -\mathbf{w}(\mathbf{x}_t, t). \quad (15)$$

While the boundary conditions in eqn (12) are common in streaming problems, its use for a sharp-edge device is problematic. Our domain has re-entrant corners at the sharp edges so that the solution of the first-order problem, while bounded, has singular velocity gradients at the sharp edges. Therefore, eqn (12) implies that, at the sharp edges, not only the velocity gradients of the second-order solution but also the velocity field itself is singular. This feature of the solution, which is intrinsic to a geometry with re-entrant corners, seems to have been neglected in other studies. In order to remove the singularity in the second-order velocity, one would have to set the displacement at the sharp edge to zero and, possibly, control its growth away from the edge. However, this constraint is difficult to justify on practical and physical grounds due to the very design of the microfluidic channel of interest. Hence, with the expectation to accurately capture the solution only outside the Stokes boundary layer, we proceed to determine numerical solutions without taking any special precautions other than the use of a reasonable adaptive mesh refinement scheme as will be described later.

3.2. Mean trajectories

Fig. 2 shows the mean trajectories of the polystyrene spherical beads placed in the fluid for streaming flow visualization purposes. As this is the primary piece of experimental evidence at our disposal, we wish to establish whether or not our calculations are able to reproduce a flow pattern similar to that in Fig. 2. The beads used in Fig. 2 are the same as those used by Bruus and co-workers[60–64] who have carefully studied the scattering problem that arises from the release of these beads within a streaming flow. We believe the results by Bruus and co-workers to be rigorous and we have implemented in our code the tracking strategy they proposed.[60–64] This strategy is predicated on the determination of the radiation force acting on a bead of radius a, mass density ρ_p, and compressibility κ_p under the influence of a standing wave in the flow. The bead is modeled as a wave scatterer, and the radiation force is then found to be

$$\mathbf{F}^{rad} = -\frac{4\pi a^3}{3}\left[\frac{1}{2}f_1\kappa_0\nabla\langle p_1^{\,2}\rangle - \frac{3}{4}\rho_0\,\mathrm{Re}(f_2)\nabla\langle \mathbf{v}_1\cdot\mathbf{v}_1\rangle\right], \quad (16)$$

where $\kappa_0 = 1/(\rho_0 c_0^{\,2})$ is the compressibility of the fluid, $\mathrm{Re}(f_2)$ is the real part of f_2, and where

$$f_1 = 1 - \frac{\kappa_p}{\kappa_0} \quad \text{and} \quad f_2 = \frac{2(1-\gamma)(\rho_p - \rho_0)}{2\rho_p + \rho_0(1-3\gamma)}, \quad (17)$$

with

$$\gamma = -\frac{3}{2}\left[1 + \imath\left(1+\tilde{\delta}\right)\right]\tilde{\delta}, \quad \tilde{\delta} = \frac{\delta}{a}, \quad \delta = \sqrt{\frac{\mu}{\pi f \rho_0}}, \quad (18)$$

and the symbol '$\imath$' denotes the imaginary unit. In addition to the radiation force, a bead is assumed to be subject to a drag force proportional to $\mathbf{v}^{bead} - \langle\mathbf{v}_2\rangle$, which is the velocity of the bead relative to the streaming velocity. When wall effects are negligible, the drag force is estimated *via* the simple formula $\mathbf{F}^{drag} = 6\pi\mu a(\langle\mathbf{v}_2\rangle - \mathbf{v}^{bead})$. The motion of the bead is then predicted *via* the application of Newton's second law:

$$m_p\mathbf{a}_p = \mathbf{F}^{rad} + \mathbf{F}^{drag}, \quad (19)$$

where m_p and $\mathbf{a}_p$ are the mass and acceleration of the bead, respectively. In many acoustofluidic problems, the inertia of the bead can be neglected.[61] Doing so, eqn (19) can be used to solve $\mathbf{v}^{bead}$:

$$\mathbf{v}^{bead} = \langle\mathbf{v}_2\rangle + \frac{\mathbf{F}^{rad}}{6\pi\mu a}. \quad (20)$$

For steady flows, we can identify the bead trajectories with the streamlines of the velocity field $\mathbf{v}^{bead}$ in eqn (20).

For an "ideal tracer", a bead should have the same density and compressibility as the surrounding fluid, $\mathbf{F}^{rad} = 0$ and the bead's velocity should coincide with the streaming velocity. However, it is well known that the trajectories of the streaming velocity field (or its streamlines in steady problems) are not fully representative of the mean trajectories of the fluid's particles as the latter are subject to a drift effect known as Stokes drift.[65] The theory around the Stokes drift is developed without reference to the motion of a bead in the fluid and therefore it can be viewed as a theory for the identification of mean trajectories of fluid particles. We adopt the theory of Lagrangian mean flow described by Bühler[66] and employed by Vanneste and Bühler,[67] in which the mean particle paths are the trajectories of a velocity field referred to as the Lagrangian velocity, denoted as $\mathbf{v}^L$, and given by

$$\mathbf{v}^L = \langle\mathbf{v}_2\rangle + \langle(\xi_1\cdot\nabla)\mathbf{v}_1\rangle, \quad (21)$$

where the field $\xi_1(\boldsymbol{x},t)$ is the first-order approximation of the lift field $\xi_1(\boldsymbol{x},t)$. The latter is defined such that $\boldsymbol{x} + \xi$ represents the true position at time t of a particle with mean position at $\boldsymbol{x}$ (also at time t). By asymptotic expansion, ξ_1 is such that

$$\frac{\partial\xi_1}{\partial t} = \mathbf{v}_1. \quad (22)$$

Eqn (22) implies that, once the first-order problem velocity solution of the form $\mathbf{v}_1 = \mathbf{v}_1^c(\mathbf{x})\,cos(2\pi ft) + \mathbf{v}_1^s(\mathbf{x})\,sin(2\pi ft)$ is computed, ξ_1 can be calculated during post-processing *via* an elementary time integration. For a steady problem, the trajectories of the fluid particles are then the streamlines of $\mathbf{v}^L$.

Different from $\mathbf{v}^{bead}$, $\mathbf{v}^L$ is an intrinsic property of the combination of the first- and second-order solutions of the acoustofluidic problem. That is, $\mathbf{v}^L$ arises from kinematic arguments alone without reference to the balance of linear momentum or the balance of mass. As such, the Lagrangian

velocity field does not coincide with either $\mathbf{v}^{\mathrm{bead}}$ or the mean velocity of the mass flow.[66,67] The latter, denoted as $\mathbf{v}^{\mathrm{M}}$, is defined such that $\rho_0\mathbf{v}^{\mathrm{M}}$ gives the second-order approximation of the linear momentum flow per unit volume:

$$\mathbf{v}^{\mathrm{M}} = \langle \mathbf{v}_2 \rangle + \frac{1}{\rho_0}\langle \rho_1 \mathbf{v}_1 \rangle. \tag{23}$$

As already alluded to, $\mathbf{v}^{\mathrm{bead}}$, $\mathbf{v}^{\mathrm{L}}$, and $\mathbf{v}^{\mathrm{M}}$ introduce corresponding notions of mean flow trajectories which can be quite distinct from one another. However, they all carry useful information about the solution.

3.3. Numerical solution approach

As is customary in acoustic streaming problems, we seek the time-harmonic solution for $\mathbf{v}_1$ and p_1 in the first-order problem, while we seek steady solutions for $\mathbf{v}_2$ and p_2 in the second-order problem. Combining information from these two solutions, it is then possible to estimate the mean trajectory of material particles in the flow.

All the solutions that will be discussed later are for two-dimensional problems. The numerical solution was obtained *via* an in-house finite element code based on the deal.II finite element library.[68,69] For both first- and second-order problems, we used $Q2$–$Q1$ elements for velocity and pressure, respectively, where $Q1$ and $Q2$ denote quadrilateral elements supporting Lagrange polynomials of order one and two, respectively. Our code was developed using the mathematical framework discussed by Köster[57] who offered a very careful analysis of the numerical properties of the approach. The main fundamental difference between our code and that by Köster is the use of adaptivity. Specifically, to mitigate somewhat the effects of the singularities discussed earlier, we adopted a very traditional adaptive mesh refinement strategy with an error estimator based on the solution's gradients.[70] Our specific error estimator was based on the gradient of the velocity solution of the first-order problem. The flow patterns we presented are those that did not significantly change upon further refinement of the mesh outside the Stokes boundary layer. Clearly, we make no claims on the values of the velocity gradients within this layer near the sharp edges.

4 Results and discussion

4.1. Constitutive parameters

All of the results presented were obtained using the values in Table 1 for the constitutive and operational parameters in the governing equations. Some of the results pertain to the motion of a dilute concentration of 1.9 μm diameter fluorescent beads. The frequency employed in simulations was chosen because it is the frequency used in prior experimental work from our group on a sharp-edge acoustic mixer with the same geometry considered herein.[41] As frequency is related to wavelength, our choice of frequency must also be consistent with the assumption discussed in section 3.1 concerning the channel being subject to a plane wave with a wavelength of roughly 30 cm. With this in mind, streaming effects in micro-acousto-fluidic devices are typically more evident at higher frequencies, *i.e.*, in the MHz regime. We have not considered such high frequencies in the present study because we feel that our assumption concerning the wave impinging on the channel would no longer be acceptable. However, for the purpose of comparison, we did carry out a simulation with a frequency of 4.75 MHz and presented the corresponding results in the ESI† (section III, Fig. 3).

Table 1 Constitutive and operational parameters

Water	
Density (ρ_0)	1000 kg m^{-3}
Shear viscosity (μ)	0.001 Pa s
Bulk viscosity (μ_b)	0.001 Pa s
Compressibility (κ_0)	448 TPa^{-1}
Speed of sound (c_0)	1500 m s^{-1}
Polystyrene beads	
Density (ρ_p)	1050 kg m^{-3}
Compressibility (κ_p)	249 TPa^{-1}
Diameter ($2a$)	1.9 μm
Operational parameters	
Forcing frequency (f)	4750 Hz
Displacement amplitude ($\|\|\mathbf{w}\|\|_{\Gamma_t,\Gamma_b}$)	1 μm

4.2. In lieu of convergence tables

As mentioned earlier, the gradients of the first-order velocity and the second-order velocity fields are unbounded at the tips of the sharp edges. As such, the second order velocity solution does not converge in a strict sense. Nonetheless, it turns out that the singularity effects are all contained within the Stokes boundary layer and it is therefore still possible to talk about an effective notion of convergence outside this layer. To illustrate this idea, we present in Fig. 4 the plots of the magnitude of the second-order velocity $\mathbf{v}_2$ as a function of position along a line parallel to the y axis (*cf.* Fig. 3), emanating from the tip of the lower sharp edge as shown in red in the left inset of Fig. 4. The latter shows three curves corresponding to increasing adaptive refinement levels identified *via* the number of degrees of freedom (DOF) used in the calculation. Our calculations have been carried out on increasingly refined meshes using the adaptive refinement strategy described in section 3.3. The left inset depicts the initial (coarsest) mesh, which consists of 4032 elements with a total of 37 251 degrees of freedom. Our most refined mesh was achieved after nine levels of adaptive refinement and it had 1 134 530 DOF. The curves shown pertain to refinement levels five, six, and seven with 248 592, 362 360, and 530 290 degrees of freedom, respectively. Curves corresponding to further refinement were not plotted because they overlapped the curves shown for refinement levels six and seven. The right inset, whose vertical axis has units identical to the overall plot, shows a zoomed-in detail of the three curves away from

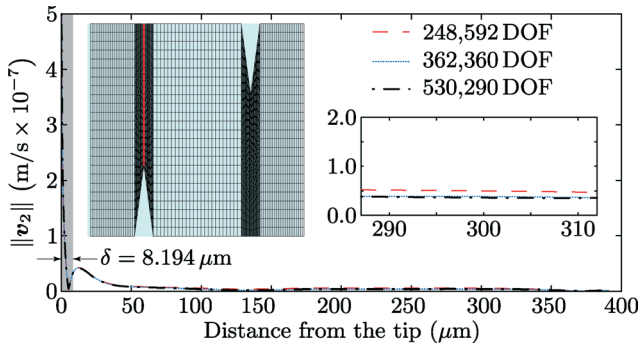

Fig. 4 Plot of the magnitude of the second-order velocity *vs.* position along a line parallel to the *y* axis and emanating from the tip of a sharp edge (red line in left inset). The different curves correspond to different levels of adaptive refinement. The inset on the left shows the initial mesh used for the calculations. The right inset shows a zoomed-in portion of the plot outside the Stokes boundary layer of thickness δ. The units on the vertical axis of the right inset are the same as those on the overall plot.

the sharp tip. To facilitate the discussion, we have used a grey rectangle at the left edge of the plot to distinguish the part of the velocity response contained in the Stokes boundary layer. The thickness of the Stokes layer has been denoted by δ and computed using the well-known formula $\delta = \sqrt{2\mu/(2\pi f \rho_0)}$.[71,72] As expected, the magnitude of $\mathbf{v}_2$ displays an asymptote at the sharp edge. At the same time, the magnitude of $\mathbf{v}_2$ appears to be well-behaved outside the Stokes layer.

4.3. Effects of boundary conditions on Γ_t and Γ_b

In section 3.1, we discussed two possible expressions for the boundary conditions on the Γ_t and Γ_b (*cf.* Fig. 3) portions of the solution's domain. Fig. 5 shows our numerical solution for the velocity $\mathbf{v}^{bead}$ in eqn (20) of beads in the flow. As shown in Fig. 3, the results in the above figure were obtained for a channel with L = 300 μm, H = 600 μm, α = 15°, and h = 200 μm. In both cases, the wall displacement was completely

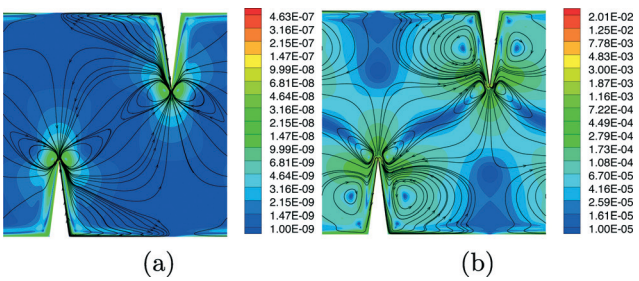

Fig. 5 Plots of the velocity $\mathbf{v}^{bead}$ in eqn (20) corresponding to the boundary conditions in (a) eqn (14) and (b) eqn (15). The color map represents the magnitude of $\mathbf{v}^{bead}$ whereas the lines are some of the streamlines of the $\mathbf{v}^{bead}$ field. The channel dimensions (*cf.* Fig. 3) are L = 300 μm, H = 600 μm, α = 15°, and h = 200 μm. The wall displacement was only in the *y* direction with magnitude 1 μm.

in the *y* direction with an amplitude of 1 μm. In both cases, we observed that eddies are predicted with streamlines symmetric relative to the (geometric) center of the simulation domain. These features match with the experimentally obtained bead traces in Fig. 2. However, we noticed that in the experiments there is no evidence of large eddies at the foot of the sharp edges, as predicted using the anti-periodic boundary conditions in eqn (15). Furthermore, we observed that the magnitude of $\mathbf{v}^{bead}$ is vastly different in the two cases. In fact, even in some regions outside the Stokes layer, the velocity predicted in Fig. 5(b) can be of the same order of magnitude as the average flow velocity observed in experiments with a net flow through the channel (absent in our simulations). Instead, the magnitudes in Fig. 5(a) are more compatible with experimental results, as are the predicted streamlines. As discussed in section 3.1, the boundary conditions used in this work are based on heuristic arguments and under the assumption that the channel is rigid, as opposed to being produced by a more sophisticated piezo-electro-elastic calculation. Despite this approximation, the result in Fig. 5(a) is very much in agreement with the experimental observations. Therefore, for the remainder of the paper, we will use only the boundary conditions in eqn (14).

4.4 Mean flows and trajectories

Next, we compare the three different types of mean velocities introduced in section 3.2, along with their corresponding streamlines. Fig. 6 shows plots of $\mathbf{v}^{bead}$, $\mathbf{v}^{L}$, and $\mathbf{v}^{M}$ for the boundary conditions given by eqn (16). Again, the channel has the following dimensions: L = 300 μm, H = 600 μm, α = 15°, and h = 200 μm; also the wall displacement was completely in the *y* direction with an amplitude of 1 μm. It is important to note that the three plots in Fig. 6 are the outcome of a single calculation, that is, they are the product of a single set of geometric parameters and boundary conditions. As discussed earlier in the paper, we view $\mathbf{v}^{bead}$ as the velocity of tracing beads in a fluid. The field $\mathbf{v}^{bead}$ is an attempt to capture, in an approximate sense, the interaction between the beads and the fluid in which they are immersed. Instead, $\mathbf{v}^{L}$, which is the sum of the second-order velocity and the Stokes drift term, is the so-called Lagrangian velocity and it is the vector field whose trajectories are the mean trajectories of the fluid particles.[66,67] Finally, $\mathbf{v}^{M}$ is the average mass flow. Fig. 6 shows that the above notions of mean flow can indeed be quite different and therefore represent very distinct properties of the same underlying solution. The difference between the streamlines of $\mathbf{v}^{L}$ and the experimental bead trajectories is expected. In fact, $\mathbf{v}^{L}$ indicates the trajectory of fluid particles in the absence of the beads in the flow, and thus should not be used for comparison with bead trajectories. On the other hand, $\mathbf{v}^{bead}$, resulting from the balance of radiation force and Stokes drag, describes the motion of the beads and is indicative of the bead trajectories observed in the experiments. We have already established that the bead trajectories are in good qualitative agreement with the

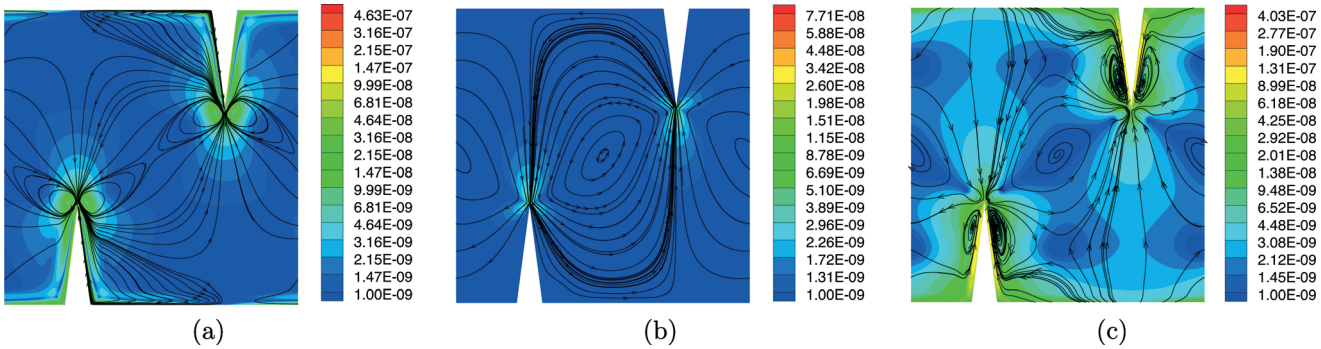

Fig. 6 Plots of the mean velocity fields and corresponding streamlines discussed in section 3.2: (a) $\mathbf{v}^{\text{bead}}$; (b) $\mathbf{v}^{\text{L}}$; (c) $\mathbf{v}^{\text{M}}$. The color map represents the velocity magnitudes, whereas the lines depict streamlines. In all cases, the channel dimensions (*cf.* Fig. 3) are L = 300 μm, H = 600 μm, α = 15°, and h = 200 μm. The wall displacement was only in the y direction with magnitude 1 μm.

experiments. Therefore, we can use the other measures of mean flow with the same degree of confidence. It may be noted from eqn (20) that the difference between $\mathbf{v}^{\text{bead}}$ and the second-order velocity depends on a term that is proportional to the square of the radius of the bead. Thus, as the bead size approaches zero, $\mathbf{v}^{\text{bead}}$ tends to the second-order velocity and the bead tracking method essentially consists of the study of the mean trajectory of the second-order velocity solution. As the velocity field $\mathbf{v}^{\text{L}}$ is an intrinsic property of the flow without any beads in it, we feel that it is a more appropriate descriptor of mean fluid particle trajectories and, as such, a more meaningful descriptor of the mixing properties of the sharp-edge device. Hence, in the remainder of the paper, we will base most of our discussion on plots of $\mathbf{v}^{\text{L}}$. Before proceeding further, we observe that the streamlines of $\mathbf{v}^{\text{L}}$ do not show eddies for the geometry and boundary conditions used to generate Fig. 6. This is because, for the stated simulation conditions, the Stokes drift effectively cancels the streaming velocity $\mathbf{v}_2$. As will be shown later, for other simulation conditions, the Lagrangian velocity will show the existence of eddies in the mean flow.

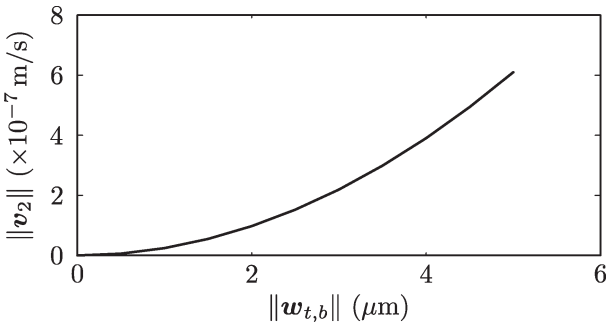

Fig. 7 Plot of the magnitude of the second-order velocity as a function of the boundary displacement amplitude. $\|\mathbf{v}_2\|$ was measured at a point lying on a line emanating from the tip of a sharp edge parallel to the y direction (*cf.* Fig. 3) and the distance away from the tip is equal to the thickness of the Stokes boundary layer. The geometry parameters have been kept the same as in preceding calculations.

4.5. Effect of displacement amplitude

Next, we study the effect of displacement amplitude prescribed on Γ_{t} and Γ_{b} on the magnitude of the resulting streaming velocity ($\mathbf{v}_2$). We simulate the acoustic streaming for different values of the input displacement amplitude and the same geometric parameters used thus far. With this in mind, Fig. 7 shows the plot of the magnitude of the second-order (streaming) velocity measured at a point lying on a line emanating from the tip of a sharp edge parallel to the y direction (*cf.* Fig. 3) and a distance away from the tip equal to the thickness of the Stokes boundary layer. The second-order streaming velocity was found to increase quadratically with displacement amplitude. This is expected since the first-order pressure and velocity depend linearly on the displacement amplitude; and the second-order streaming velocity, in turn, depends quadratically on the first-order pressure and velocity. In the experiments, the amplitude of the acoustic wave is proportional to the square-root of the signal power, for small values of the signal power. Thus, we expect the streaming velocity to be linearly dependent on the input signal power.

4.6. Effect of the channel dimensions h and H

In this section, we turn to an assessment of the effectiveness of sharp edges in acoustofluidic mixing. Mixing characterization is an inherently complex subject because mixing is a time dependent process. The assessment offered in this paper is limited to the theoretical modeling employed: the equations presented earlier are for a single flow. Therefore, our conclusions are strictly applicable only to perfectly miscible fluids of same density and constitutive properties. Because our focus is on the analysis of steady state acoustic streaming, we did not consider the time evolution of the fluid. This is not to say that our predictions are inadequate. In fact, analyzing the structure of steady state mean particle trajectories is analogous to analyzing a dynamical system's response in phase-space to determine the possible evolution of the system as a function of initial conditions, where the latter, in the present context, is the initial positions of fluid

particles in the channel. Therefore, given fluid particles initially distributed as shown in Fig. 1(a) near the fluid inlets, we can tell whether or not particles are forced by the device to travel away from their initial position. While we do not solve a time dependent system, we do solve for the streaming velocity. This indicator will allow us to assess whether a particular configuration will achieve mixing more rapidly than the other. The mean trajectories we study are the streamlines of the Lagrangian velocity field $\mathbf{v}^L$.

As shown in Fig. 3, we begin our analysis by considering the effect of the channel dimensions h and H. We consider three different cases with constant tip size h = 200 μm and the following values for H: 600 μm, 750 μm, and 900 μm. In all cases, the separation between sharp edges L was 300 μm and the tip angle α was 15°. It can be seen from Fig. 8, regardless of the ratio h/H, that fluid particles near the walls are forced by the device to travel towards the opposite wall. Also, as the ratio h/H decreases, the flow pattern "breaks" into two distinct vortices, thus acquiring the sort of pattern displayed in Fig. 5. This result indicates that there is a critical value of h/H for which eddies might not be present. Unfortunately, we do not have experimental confirmation of this finding at this time. Nonetheless, this finding points to the conclusion that narrowing channels might not be necessarily desirable. We view the presence of eddies near the oscillating sharp tips as a mixing enhancer. This feature indicates that there are trajectories spanning the entire width of the channel in close proximity with trajectories of a very different type, namely with local circulation. While this pattern is certainly not turbulent or chaotic, it does indicate the possibility of good mixing conditions in that a small local random perturbation around the oscillating tips can cause particles coming from, say, the top region of the domain to be "trapped" (at least temporarily) in a completely different region of the channel. From the viewpoint of mixing with an underlying input flow, the fact that the streaming flow solution displays a very distinct central symmetry indicates that better mixing conditions are achieved by ensuring that the inlet flow is not centered within the channel. Finally, we observe that, as H increases, the fraction of the solution domain experiencing mid-range velocity magnitudes appears to increase.

4.7. Effect of the channel dimension L

As shown in Fig. 3, L is the distance separating sharp edges on opposite sides of the channel walls. Fig. 9 shows the Lagrange velocity streamlines and magnitudes for three different values of the parameter L equal to 200 μm, 300 μm, and 400 μm. The values of h and H were 200 μm and 600 μm, respectively. The tip angle was set to 15°. These results indicate that increasing the distance between opposing sharp edges does not favor the presence of eddies near the tips. However, the streamlines in Fig. 9(a) seem to indicate the presence of possible stagnation points at the feet of the sharp edges, clearly a feature that would be undesirable. As far as the magnitude of the velocity is concerned, the figures do not indicate sufficiently strong trends in this regard.

4.8. Effect of tip angle

Normally, mixing of fluids occurs as these fluids move along the channel. That is, when there is a net flow, governed by the conditions at the inlets, it interacts with the streaming flow. Provided that we did not consider this interaction, the ability of the device to force particles along the trajectories illustrated thus far depends on the strength of the streaming flow in relation to the background net motion along the channel. For this reason, it is important to determine which, if any, is the design feature that most decisively contributes to the magnitude of the streaming flow. We believe this feature to be the angle α (*cf.* Fig. 3) at the tip of the sharp edge. It is because α is acute that the second-order solution is singular. It is therefore important to understand how α affects

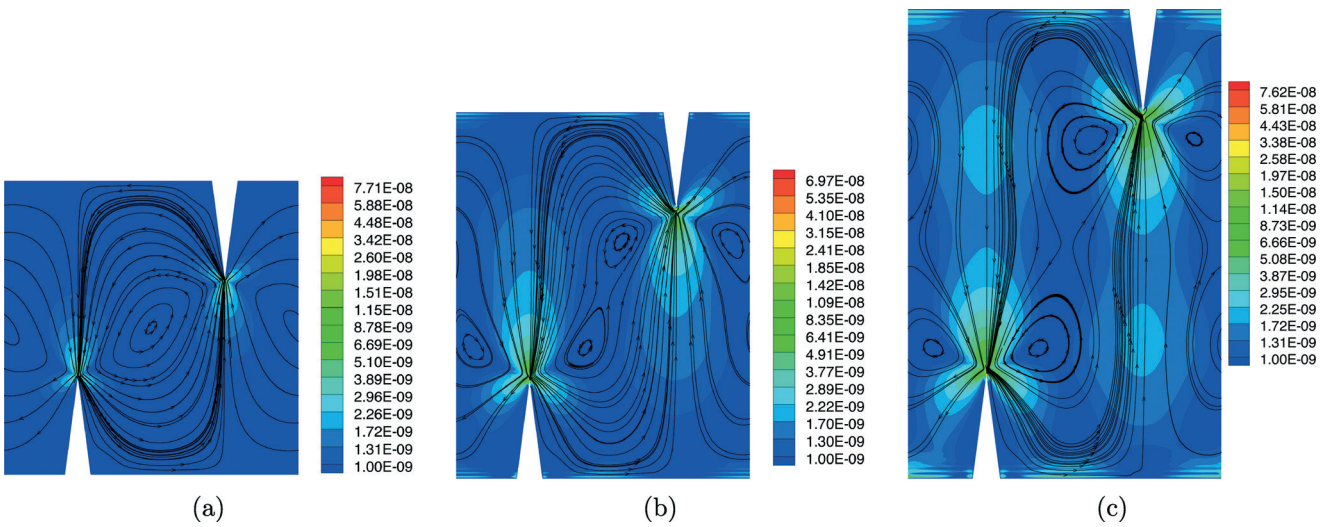

Fig. 8 Plots particle trajectories for three different cases with fixed value of h = 200 μm and values of (a) H = 600 μm, (b) 750 μm, and (c) 900 μm (*cf.* Fig. 3). The color map describes the values of the magnitude of the Lagrangian velocity $\mathbf{v}^L$, whereas the lines identify the streamlines of $\mathbf{v}^L$.

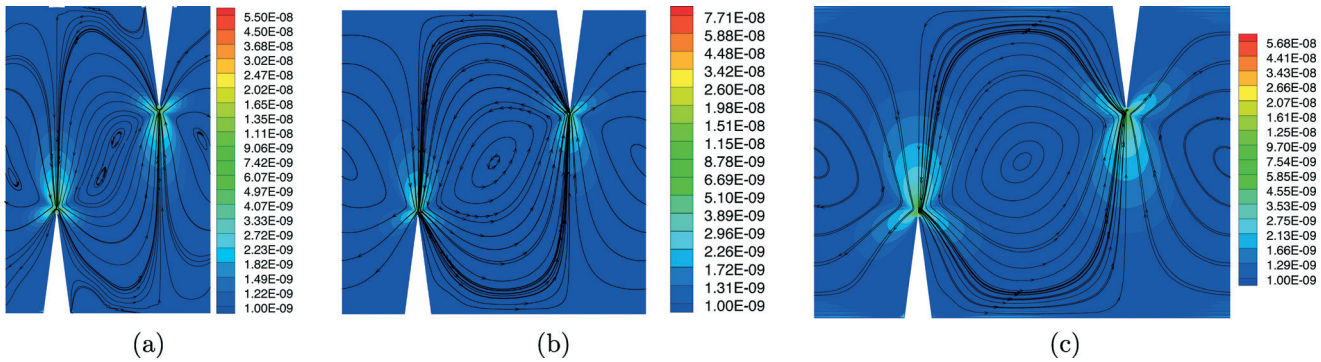

Fig. 9 Plots particle trajectories for three different cases with fixed values of h = 200 μm and H = 600 μm, and different values of (a) L = 200 μm, (b) 300 μm, and (c) 400 μm (*cf.* Fig. 3). The color map describes the values of the magnitude of the Lagrangian velocity $\mathbf{v}^L$, whereas the lines identify the streamlines of $\mathbf{v}^L$.

the strength of the streaming flow. Normally, one would have to characterize the type of singularity induced by the tip angle and make inferences on the overall strength of the streaming flow. Unfortunately, no analytical results are available on the analysis of the strength of the singularity at re-entrant corners for asymptotic expansions of the compressible Navier–Stokes equations as employed here. However, in the equations for both the first- and second-order problems, we see the presence of differential operators that are strongly reminiscent of the Navier equations for the linear elastic boundary value problem.

When a re-entrant corner is present in elastic problems, the displacement gradient experiences singularities of the type $1/r^c$, where r is the distance from the tip of the corner and $0 < \lambda < \frac{1}{2}$.[73] For $\alpha \to 0$, $\lambda \to \frac{1}{2}$, which represents the stress/strain behavior found at the tip of a sharp crack. While the equations used herein are not identical to those of linear elasto-statics, we speculate that the analogy with fracture problems in elasticity might be an appropriate tool to guide us in the interpretation of the results. In order to quantify how the velocity depends on the tip angle, we have measured the magnitude of $\mathbf{v}_2$ at a distance equal to 2δ ahead of the tip along a line emanating from the tip and parallel to the y, where δ is the thickness of the Stokes layer. The calculations are reported in Fig. 10. Clearly, the choice of location at which $||\mathbf{v}_2||$ is measured is arbitrary but it is motivated by the fact that $||\mathbf{v}_2||$ becomes unbounded as the tip is approached and therefore its measure becomes meaningless. The plot shows that $||\mathbf{v}_2||$ increases with a decrease of tip angle and that the rate of increase also increases as α becomes smaller. Hence, one immediate conclusion is that the smaller the value of α, the stronger the effect of the streaming flow on the overall flow in the device and the better its mixing properties. However, this conclusion needs to be tested by considering the effect of the tip angle on particle trajectories. This effect was captured in Fig. 11 for the values of tip angles already mentioned. What is important to notice is that, for α = 7.5° the simulation predicts the appearance of recirculation areas at the feet of the sharp edges that may trap fluid particles permanently. This effect is not entirely surprising since

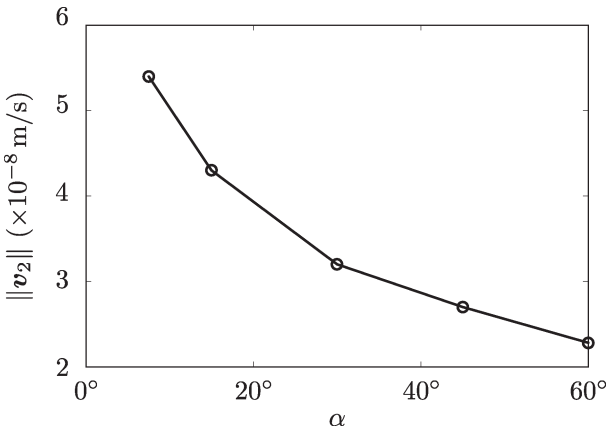

Fig. 10 Plot of $||\mathbf{v}_2||$ values at a fixed point ahead of a sharp edge *vs.* tip angle α (*cf.* Fig. 3). The dimensions of the channel are h = 200 μm, H = 600 μm and L = 300 μm. Open circles denote computed data points corresponding to α = 7.5°, 15°, 30°, 45°, and 60°. In all cases, $||\mathbf{v}_2||$ was calculated at the point lying on a line emanating from the tip of a sharp edge parallel to the y direction and the distance away from the tip is equal to twice the thickness of the Stokes boundary layer.

the angle at the sharp edge feet reaches 90° as α reaches zero, thus producing stagnation zones in the channel with adverse effect on the device mixing properties. At the same time, we notice that, as the angle becomes smaller, higher values of particle velocity are present over a larger portion of the solution domain. The importance of this observation lies in the fact that higher particle velocities can strongly reduce mixing times and therefore have a very enhancing effect on the mixing properties of the device as a whole.

5 Conclusion

We studied the flow around acoustically actuated oscillating sharp edges inside a microchannel using a perturbation approach. The numerical results were compared with experimental results and a very good agreement was observed between them, especially in view of the strong simplifying assumptions adopted in choosing boundary conditions. We demonstrated that a computational domain under periodic

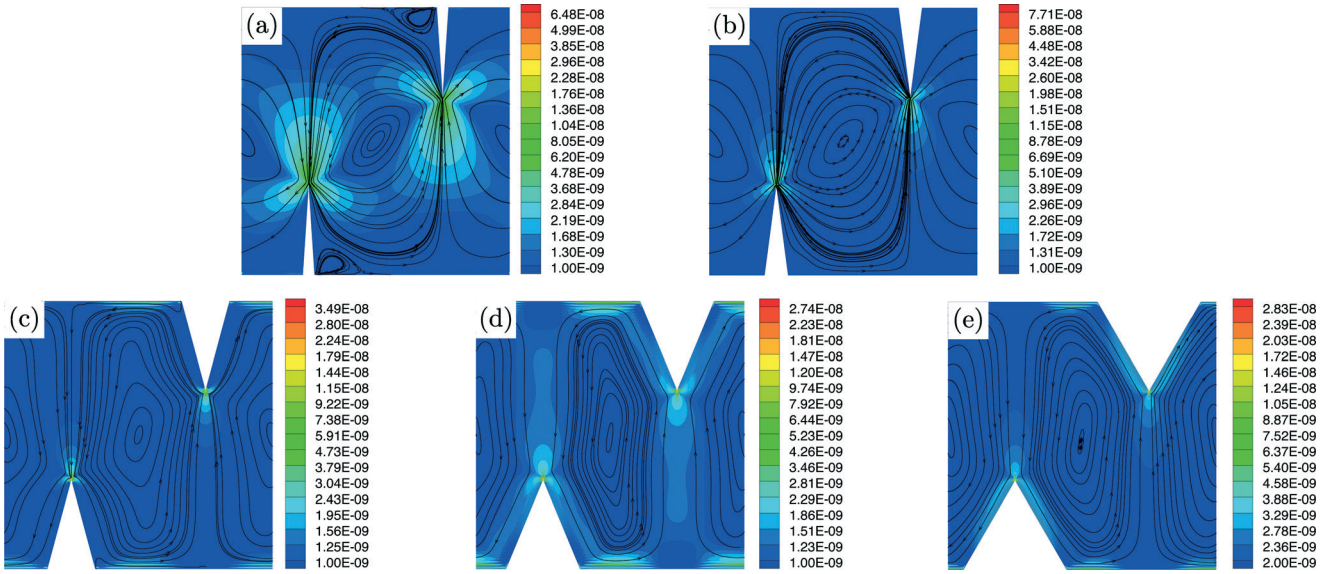

Fig. 11 Plot of $||\mathbf{v}^{L}||$ (colormap) and it streamlines for various values of tip angle α (*cf.* Fig. 3). The dimensions of the channel are h = 200 μm, H = 600 μm and L = 300 μm. The values of α are (a) 7.5°, (b) 15°, (c) 30°, (d) 45°, and (e) 60°.

boundary conditions can be used to model the full device, resulting in significant savings in computational costs and time. The predicted flow profiles were found to reflect the inherent nonlinearity of the acoustic streaming phenomenon as the various patterns identified are not linear scaling of one another. The flow field was found to be heavily dependent on the geometrical parameters of the device like the tip angle of the sharp edges and the ratio h/H between the distance of the sharp edges from the wall and the overall channel's width. The streaming velocity was also observed to show a quadratic dependence on the applied input displacement and a nonlinear increase with the decrease in the tip angle. At the same time, we showed that properties contributing to the overall mixing effectiveness of the device can be in "competition" with each other, making the identification of the optimal geometric and working configurations nontrivial. For this reason, we believe that our computational effort, in addition to providing better understanding of flow around sharp edges in confined microchannels, is also very useful in design optimization of sharp-edge micro-mixers. The latter have numerous applications in many lab-on-a chip processes like medical diagnostics, drug delivery, chemical synthesis, and enzyme reactions.[74–76] A natural extension of our numerical model would be to include the coupling of the microfluidic channel with the substrate. Our numerical model can also be integrated with a study of the acoustic wave propagation through phononic structures which have been recently demonstrated[77–79] as an alternative interface between the substrate and the disposable microfluidic chip to achieve better control of the acoustic wave propagation.

Acknowledgements

We gratefully acknowledge financial support from the National Institutes of Health (Director's New Innovator Award, 1DP2OD007209-01), American Asthma Foundation (AAF) Scholar Award, and the Penn State Center for Nanoscale Science (MRSEC) under grant DMR-0820404.

References

1 A. Lee, *Lab Chip*, 2013, **13**, 1660–1661.
2 J. T. Coleman and D. Sinton, *Microfluid. Nanofluid.*, 2005, **1**, 319–327.
3 S. S. Wang, X. Y. Huang and C. Yang, *Lab Chip*, 2011, **11**, 2081–2087.
4 A. D. Stroock, S. K. W. Dertinger, A. Ajdari, I. Mezić, H. A. Stone and G. M. Whitesides, *Science*, 2002, **295**, 647–651.
5 H. Chen and J.-C. Meiners, *Appl. Phys. Lett.*, 2004, **84**, 2193–2195.
6 Y.-K. Lee, C. Shih, P. Tabeling and C.-M. Ho, *J. Fluid Mech.*, 2007, **575**, 425–448.
7 Y.-C. Lin, Y.-C. Chung and C.-Y. Wu, *Biomed. Microdevices*, 2007, **9**, 215–221.
8 Z. Z. Che, N.-T. Nguyen and T. N. Wong, *Phys. Rev. E: Stat., Nonlinear, Soft Matter Phys.*, 2011, **84**, 066309.
9 C. H. Hsu and A. Folch, *Appl. Phys. Lett.*, 2006, **89**, 144102.
10 H. Y. Park, X. Qiu, E. Rhoades, J. Korlach, L. W. Kwok, W. R. Zipfel, W. W. Webb and L. Pollack, *Anal. Chem.*, 2006, **78**, 4465–4473.
11 X. Mao, J. R. Waldeisen and T. J. Huang, *Lab Chip*, 2007, **7**, 1260–1262.
12 C.-Y. Lee, G.-B. Lee, L.-M. Fu, K.-H. Lee and R.-J. Yang, *J. Micromech. Microeng.*, 2004, **14**, 1390–1398.
13 C. K. Harnett, J. Templeton, K. A. Dunphy-Guzman, Y. M. Senousy and M. P. Kanouff, *Lab Chip*, 2008, **8**, 565–572.
14 M. Sigurdson, D. Wang and C. D. Meinhart, *Lab Chip*, 2005, **5**, 1366–1373.

15 W. Y. Ng, S. Goh, Y. C. Lam, C. Yang and I. Rodríguez, *Lab Chip*, 2009, **9**, 802–809.
16 J. T. Coleman, J. McKechnie and D. Sinton, *Lab Chip*, 2006, **6**, 1033–1039.
17 C. Neils, Z. Tyree, B. Finlayson and A. Folch, *Lab Chip*, 2004, **4**, 342–350.
18 T. W. Lim, Y. Son, Y. J. Jeong, D.-Y. Yang, H.-J. Kong, K.-S. Lee and D.-P. Kim, *Lab Chip*, 2011, **11**, 100–103.
19 J.-H. Tsai and L. Lin, *Sens. Actuators, A*, 2002, **97–98**, 665–671.
20 B. Xu, T. N. Wong, N.-T. Nguyen, Z. Z. Che and J. C. K. Chai, *Biomicrofluidics*, 2010, **4**, 044102.
21 A. N. Hellman, K. R. Rau, H. H. Yoon, S. Bae, J. F. Palmer, K. S. Phillips, N. L. Allbritton and V. Venugopalan, *Anal. Chem.*, 2007, **79**, 4484–4492.
22 S.-C. S. Lin, X. Mao and T. J. Huang, *Lab Chip*, 2012, **12**, 2766–2770.
23 J. Shi, X. Mao, D. Ahmed, A. Colletti and T. J. Huang, *Lab Chip*, 2008, **8**, 221–223.
24 A. R. Rezk, A. Qi, J. R. Friend, W. H. Li and L. Y. Yeo, *Lab Chip*, 2012, **12**, 773–779.
25 W.-K. Tseng, J.-L. Lin, W.-C. Sung, S.-H. Chen and G.-B. Lee, *J. Micromech. Microeng.*, 2006, **16**, 539–548.
26 T.-D. Luong, V.-N. Phan and N.-T. Nguyen, *Microfluid. Nanofluid.*, 2011, **10**, 619–625.
27 A. Wixforth, C. Strobl, C. Gauer, A. Toegl, J. Scriba and Z. von Guttenberg, *Anal. Bioanal. Chem.*, 2004, **379**, 982–991.
28 T. Frommelt, M. Kostur, M. Wenzel-Schäfer, P. Talkner, P. Hänggi and A. Wixforth, *Phys. Rev. Lett.*, 2008, **100**, 034502.
29 K. Sritharan, C. J. Strobl, M. F. Schneider, A. Wixforth and Z. Guttenberg, *Appl. Phys. Lett.*, 2006, **88**, 054102.
30 H. Yu, J. W. Kwon and E. S. Kim, *J. Microelectromech. Syst.*, 2006, **15**, 1015–1024.
31 Z. Yang, S. Matsumoto, H. Goto, M. Matsumoto and R. Maeda, *Sens. Actuators, A*, 2001, **93**, 266–272.
32 S. Oberti, A. Neild and T. W. Ng, *Lab Chip*, 2009, **9**, 1435–1438.
33 D. Ahmed, X. Mao, B. K. Juluri and T. J. Huang, *Microfluid. Nanofluid.*, 2009, **7**, 727–731.
34 J. Collin, J. Fan, R. Moghbel, A.-H. Hsieh and A. Lee, *Proceeding of The Tenth International Conference on Miniaturized Systems for Chemistry and Life Sciences (μTAS 2006)*, 2006, pp. 116–118.
35 R. H. Liu, J. N. Yang, M. Z. Pindera, M. Athavale and P. Grodzinski, *Lab Chip*, 2002, **2**, 151–157.
36 Y. Xie, D. Ahmed, M. I. Lapsley, S.-C. S. Lin, A. A. Nawaz, L. Wang and T. J. Huang, *Anal. Chem.*, 2012, **84**, 7495–7501.
37 R. H. Liu, J. Yang, M. Z. Pindera, M. Athavale and P. Grodzinski, *Lab Chip*, 2002, **2**, 151–157.
38 K. Rodaree, T. Maturos, S. Chaotheing, T. Pogfay, N. Suwanakitti, C. Wongsombat, K. Jaruwongrungsee, A. Wisitsoraat, S. Kamchonwongpaisan, T. Lomas and A. Tuantranont, *Lab Chip*, 2011, **11**, 1059–1064.
39 D. Ahmed, C. Y. Chan, S.-C. S. Lin, H. S. Muddana, N. Nama, S. J. Benkovic and T. J. Huang, *Lab Chip*, 2013, **13**, 328–331.
40 P.-H. Huang, M. I. Lapsley, D. Ahmed, Y. Chen, L. Wang and T. J. Huang, *Appl. Phys. Lett.*, 2012, **101**, 141101.
41 P.-H. Huang, Y. Xie, D. Ahmed, J. Rufo, N. Nama, Y. Chen, C. Y. Chan and T. J. Huang, *Lab Chip*, 2013, **13**, 3847–3852.
42 C. Chindam, N. Nama, M. I. Lapsley, F. Costanzo and T. J. Huang, *J. Appl. Phys.*, 2013, **114**, 194503.
43 N. Riley, *Theor. Comput. Fluid Dyn.*, 1998, **10**, 349–356.
44 N. Riley, *Annu. Rev. Fluid Mech.*, 2001, **33**, 43–65.
45 J. Lighthill, *Journal of Sound and Vibration*, 1978, **61**, 391–418.
46 A. Bertelsen, A. Svardal and S. Tjøtta, *J. Fluid Mech.*, 1973, **59**, 493–511.
47 H. Bruus, J. Dual, J. Hawkes, M. Hill, T. Laurell, J. Nilsson, S. Radel, S. Sadhal and M. Wiklund, *Lab Chip*, 2011, **11**, 3579–3580.
48 X. Ding, P. Li, S.-C. S. Lin, Z. S. Stratton, N. Nama, F. Guo, D. Slotcavage, X. Mao, J. Shi, F. Costanzo and T. J. Huang, *Lab Chip*, 2013, **13**, 3626–3649.
49 V. H. Lieu, T. A. House and D. T. Schwartz, *Anal. Chem.*, 2012, **84**, 1963–1968.
50 K. D. Frampton, S. E. Martin and K. Minor, *Applied Acoustics*, 2003, **64**, 681–692.
51 W. L. Nyborg, in *Nonlinear Acoustics*, ed. M. F. Hamilton and D. T. Blackstock, Academic Press, San Diego, CA, 1998, pp. 207–231.
52 D. Ahmed, X. Mao, J. Shi, B. K. Juluri and T. J. Huang, *Lab Chip*, 2009, **9**, 2738–2741.
53 X. Mao, B. K. Juluri, M. I. Lapsley, Z. S. Stratton and T. J. Huang, *Microfluid. Nanofluid.*, 2009, **8**, 139–144.
54 M. E. Gurtin, E. Fried and L. Anand, *The Mechanics and Thermodynamics of Continua*, Cambridge University Press, New York, 2010.
55 S. S. Sadhal, *Lab Chip*, 2012, **12**, 2292–2300.
56 T. Frommelt, D. Gogel, M. Kostur, P. Talkner, P. Hänggi and A. Wixforth, *IEEE Trans. Ultrason., Ferroelectr., Freq. Control*, 2008, **55**, 2298–2305.
57 D. Köster, *Ph.D. thesis*, Universität Augsburg, Germany, 2006.
58 J. T. Stuart, *J. Fluid Mech.*, 1966, **24**, 673–687.
59 C. E. Bradley, *J. Acoust. Soc. Am.*, 1996, **100**, 1399–1408.
60 H. Bruus, *Lab Chip*, 2012, **12**, 1014–1021.
61 R. Barnkob, *Ph.D. thesis*, Danmarks Tekniske Universitet (DTU), Lyngby, Denmark, 2012.
62 P. B. Muller, R. Barnkob, M. J. H. Jensen and H. Bruus, *Lab Chip*, 2012, **12**, 4617–4627.
63 M. Settnes and H. Bruus, *Phys. Rev. E: Stat., Nonlinear, Soft Matter Phys.*, 2012, **85**, 016327.
64 R. Barnkob, P. Augustsson, T. Laurell and H. Bruus, *Phys. Rev. E: Stat., Nonlinear, Soft Matter Phys.*, 2012, **86**, 056307.
65 L. K. Zarembo, in *High-Intensity Ultrasonic Fields*, ed. L. D. Rozenberg, Springer, 1971, pp. 135–199.
66 O. Bühler, *Waves and Mean Flows*, Cambridge University Press, Cambridge, UK, 2009.
67 J. Vanneste and O. Bühler, *Proc. R. Soc. A*, 2011, **467**, 1779–1800.
68 W. Bangerth, R. Hartmann and G. Kanschat, *ACM Transactions on Mathematical Software (TOMS)*, 2007, **33**, 24.
69 W. Bangerth, R. Hartmann and G. Kanschat, *deal.II Differential Equations Analysis Library*, 1998–2006.

70 D. W. Kelly, J. P. D. S. R. Gago, O. C. Zienkiewicz and I. Babuska, *International Journal for Numerical Methods in Engineering*, 1983, **19**, 1593–1619.
71 J. J. Lei, P. Glynne-Jones and M. Hill, *Lab Chip*, 2013, **13**, 2133–2143.
72 J. J. Lei, M. Hill and P. Glynne-Jones, *Lab Chip*, 2014, **14**, 532–541.
73 M. H. Sadd, *Elasticity: Theory, Applications, and Numerics*, Elsevier Academic Press Inc., 2nd edn, 2009.
74 S. Yang, F. Guo, B. Kiraly, X. Mao, M. Lu and T. J. Huang, *Lab Chip*, 2012, **12**, 2097–2102.
75 P. Neuzil, S. Giselbrecht, K. Lnge, T. J. Huang and A. Manz, *Nat. Rev. Drug Discovery*, 2012, **11**, 620–632.
76 X. Mao and T. J. Huang, *Lab Chip*, 2012, **12**, 1412–1416.
77 R. Wilson, J. Reboud, Y. Bourquin, S. L. Neale, Y. Zhang and J. M. Cooper, *Lab Chip*, 2011, **11**, 323–328.
78 Y. Bourquin, R. Wilson, Y. Zhang, J. Reboud and J. M. Cooper, *Adv. Mater.*, 2011, **23**, 1458–1462.
79 J. Reboud, R. Wilson, Y. Zhang, M. H. Ismail, Y. Bourquin and J. M. Cooper, *Lab Chip*, 2012, **12**, 1268–1273.

